



Study on microstructure evolution and mechanical properties of high-strength low-alloy steel welds realized by flash butt welding thermomechanical simulation

Jun Wang¹ · Yao Lu¹ · Jian Han¹ · Jianjun Qi² · Li Sun² · Zhengyi Jiang¹ · Cheng Ma² · Valerie Linton¹

Received: 7 April 2022 / Accepted: 26 July 2022 / Published online: 13 August 2022
© The Author(s) 2022

Abstract

Defects would occur in the weld joint of the wheel rims during the post-flash butt welding (FBW) process suffering from poor plasticity, which will deteriorate the quality and lifecycle of finish products. Therefore, the FBW process of the 440CL high-strength-low-alloy (HSLA) steel was physically simulated and the influence of flash parameters on FBW joints was systematically evaluated in this study. The results showed that the width of heat affected zone increased with accumulated flash allowance (δ_f) while declined with accelerated flash speed (v_f). The recrystallization level would be intensified with increased δ_f . Meanwhile, the acceleration in v_f populated the WZ with a more homogeneous microstructure, higher recrystallization degree and lower dislocation density. The hardness in WZ slightly reduced (202 → 195 HV) as increased δ_f but obviously dropped (192 → 177 HV) as increased v_f . All tensile samples were fractured at the BM location and the tensile properties of FBW joints exhibit a good match with those of BM, with a slight increase in strength (UTS: 468 ~ 493 MPa; YS: 370 ~ 403 MPa) but a mild decrease in plasticity (EL: 39 ~ 44%; RA: 74 ~ 79%). Furthermore, both the joint strength and ductility showed a downward tendency with the increment of δ_f . However, the strength slightly decreased while the ductility increased with the advancement of v_f . These findings would be valuably referential to the real FBW of HSLA steels with optimized microstructure and mechanical performance.

Keywords Flash butt welding · Flash parameters · Thermodynamic cycles · Microstructure · Mechanical properties

Abbreviations

FBW	Flash butt welding	P	Pearlite
CGHAZ	Coarse-grain heat affected zone	BM	Base metal
PF	Primary ferrite	SEM	Scanning electron microscope
AF	Acicular ferrite	GBMA	Grain boundary misorientation angle
WZ	Weld interface zone	PA	Prior austenite
v_f	Flash speed	EL	Elongation
LAGBs	Low-angle grain boundaries	UTS	Ultimate tensile strength
		HSLA	High-strength-low-alloy
		FGHAZ	Fine-grain heat affected zone
		WF	Widmanstätten ferrite
		BF	Bainite ferrite
		δ_f	Flash allowance
		HAGBs	High-angle grain boundaries
		F	Ferrite
		RD	Rolling direction
		OM	Optical microscope
		EBSD	Electron backscatter diffraction
		GNDs	Geometrically necessary dislocations
		IPF	Inverse pole figure
		YS	Yield strength

✉ Zhengyi Jiang
jiang@uow.edu.au

✉ Cheng Ma
macheng01@hbisco.com

✉ Valerie Linton
v.linton@auckland.ac.nz

¹ School of Mechanical, Materials, Mechatronic and Biomedical Engineering, University of Wollongong, Wollongong, NSW 2522, Australia

² Technology Research Institute, HBIS Group, Shijiazhuang 050023, China

1 Introduction

As an important part of resistance welding technology, the flash butt welding (FBW) process is extensively applied in transportation and oil pipeline industries, including joining railway tracks, automotive wheel rims, vessel mooring chains and line pipes [1–4]. During the FBW process, the contact surfaces of workpieces will be rapidly heated to melt and join through resistance heat generated by the heavy transient current, while one side is fixed, and the other side is tightened by a movable clamp for subsequent upset action. Once the metal behind the contact surface has been sufficiently heated to guarantee adequate plasticity, the flash current will be stopped and the movable clamp will apply greater force to butt the contact surfaces together so that the molten oxides and impurities could be squeezed out of the joint [2, 5–7]. Theoretically speaking, FBW is a combination of melting and forging processes that produce welded joints with superior mechanical performances comparable to the base metal, as well as possesses various advantages of high welding efficiency, sound welding formability, and is independent of additional filler wire [8–10].

In the past few decades, with the continuous advancement of production technology and the overall enhancement of safety and environmental awareness, the automobile lightweight become the focus of the entire automotive industry [11]. Consequently, the expectation of improving material performance, energy efficiency and cost-effectiveness has become the overall goal of the automotive industry. The application of high-strength low-alloy (HSLA) steel is very extensive and indispensable in the automotive lightweight industry especially for the application of truck wheel rims, benefiting from their performance characteristics including high strength and toughness, superior resistance to brittle fracture and corrosion [12–16]. As an efficient and commonly used joint operation, FBW technology exerts a vital influence in determining the forming quality and service life in the manufacture of automobile rims. Thereinto, the variation of key welding parameters is the crucial factor directly affecting the microstructural evolution and mechanical performance of the FBW joints. Ziemian et al. [17] evaluated the significance of flash and upset sequences on microstructure, inclusion and mechanical characteristics of ASTM A529-Grade 50 steel FBW weld joints. The strength and defects of the welds are highlighted to be sensitive to parameters of flash duration, upset allowance and current. Shi et al. [18] comprehensively studied the influence of upset allowances on the quantities of inclusions with flash welding duration fixed and revealed that excessively short and long upset allowance will exert a detrimental effect on the breaking force. Siddiqui et al. [5] developed a computational fluid dynamics-based model to analyse the alumina inclusion behaviour

during AC flash welding and found that the whole inclusion motion would be significantly affected by upsetting parameters. Wang et al. [19] the effects of the electrode feeding mode on the heating uniformity of the end face through a combination of numerical simulation and experiment and demonstrated that the skin effect is prominent once the AC passes through the low-temperature variation zone. Xi et al. [9, 20] systematically investigated the influence of flash and upset allowances on the characteristics of RS590CL welds and recommended the optimal range for obtaining high-quality FBW joints. Lu et al. [21] assessed the effect of FBW parameters on the microstructures, mechanical properties and post-formability of B590CL welded joints and the fracture mechanisms in the practical production of the B590CL wheel rims. Shajan et al. [22, 23] established the correction between the upset pressure, texture evolution and toughness of the micro-alloyed flash butt joints, providing a new perspective to explain how the upset pressure impacts the final performance. Shajan et al. [24] investigated the effects of post-heat treatment on the microstructure and toughness of FBW HSLA steel and found that recrystallization could be effectively induced by applying 1000 °C for a duration of 5 s, contributing to an improvement in weld zone toughness. On the whole, the above investigations imply that the influence of parameters on the performance of FBW joints is mainly realized by affecting the thermodynamic cycles.

During the wheel rim production process, cracks or thinning would occur in the weld joints in the post-weld process including bulging and flaring suffering from poor plasticity, which will deteriorate the quality and lifecycle of finish products. The abovementioned issue would be predominant with the increase in steel strength grades. In this investigation, a physical simulation method was utilized to study the microstructural and mechanical evolution of the flash butt-welded HSLA steel because it features a reduction in work time and raw material, and it will not disturb the site production. To visually present the differences in thermodynamic cycles with the variation of parameters, FBW processes of HSLA steels with different flash parameters were conducted on Gleeble 3500 thermomechanical simulator. The purpose of the present investigation is to evaluate the influence of flash allowance and speed on the thermodynamic cycles, microstructure and mechanical performance of 440CL welds by controlling variables.

2 Experimental

2.1 Raw material

In this investigation, commercial hot-rolled 440CL strips (material standards: JT020-2015 and YB/T 4151–2006) with a thickness of 6 mm were utilized as raw materials.

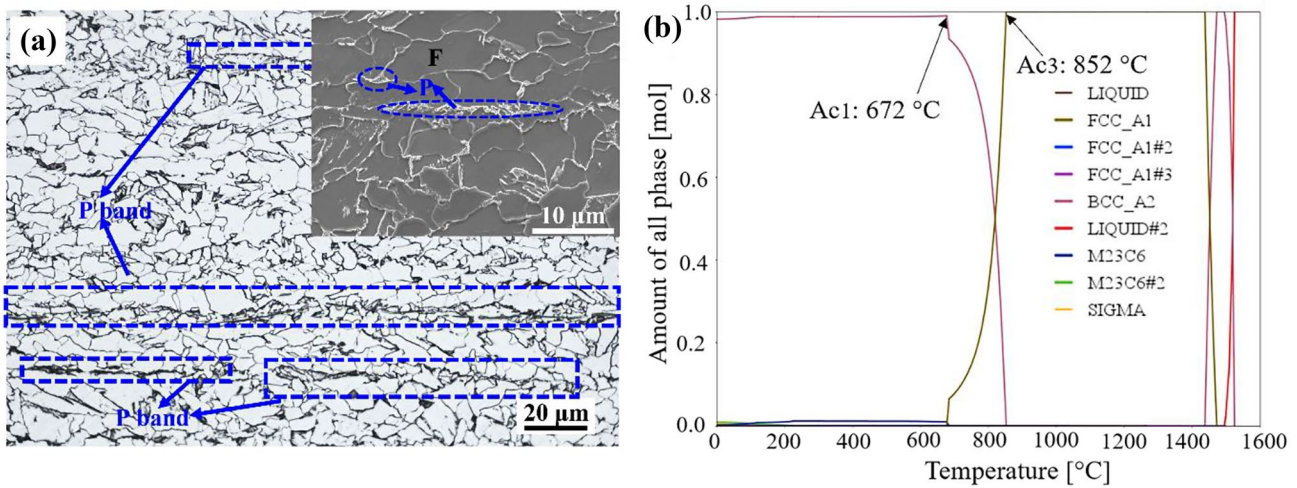


Fig. 1 a As-received microstructure, and b calculated phase diagram of the 440CL HSLA steel

The microstructure and phase diagram of the aforementioned material are shown in Fig. 1a, b, respectively. The as-received microstructure consists of major F (ferrite) and minor P (pearlite). P band structure formed along the rolling direction (RD), mainly derived from dendritic segregation and carbon enrichment in the molten status and then stretched along RD during the rolling process. Through the phase diagram calculated by Thermo calc software, the Ac_1 and Ac_3 temperatures were estimated to be 672 °C and 852 °C, respectively. The chemical composition is listed in Table 1.

2.2 FBW physical simulation process

The FBW experiments were conducted on Gleeble 3500 thermo-mechanical simulator, as shown in Fig. 2a. Figure 2b shows how a pair of specimens with a dimension of 70 mm × 10 mm × 6 mm (length × width × thickness) were assembled with clamps in this simulator. To accurately simulate the real welding process, the thermal cycle was controlled through spot-welded thermocouples 10 mm away from the contact surface. During the FBW process, sample pairs were firstly heated to 1250 °C with a heating rate of 250 K/s and then went through flash and upset steps in sequence, followed by air cooling. These parameters are from the data collected by the flash butt welding company on-site and provided by HBIS group. To separately evaluate the effects of flash allowance (δ_f) and flash speed (v_f) on the

thermomechanical cycle, weld formability, microstructure evolution and mechanical properties of welded joints, 4 sets of pairs were welded using different δ_f values ranging from 6 to 12 mm, and 5 sets of pairs were welded by varied v_f values from 1 to 9 mm/s, while other key parameters were kept constant referring to the actual FBW situation. Table 2 summarizes the parameter details of each experimental set. Note that each set of tests was repeated four times to obtain four FBW joints, one for microstructural and hardness detection, and the others for tensile tests.

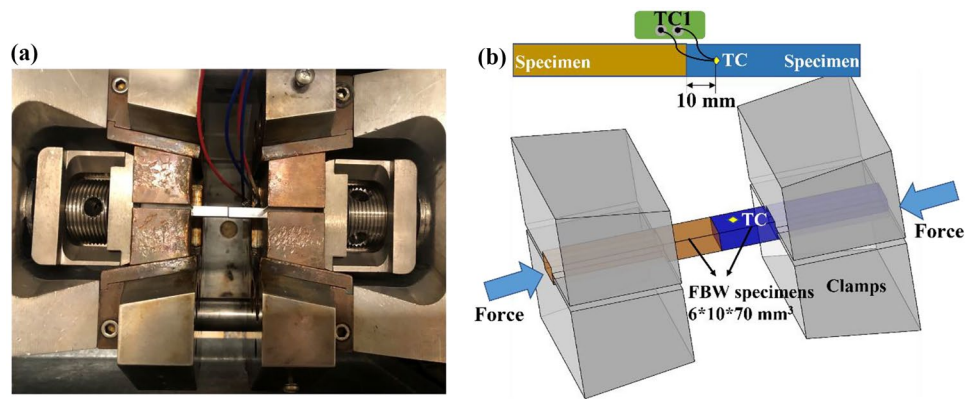
2.3 Characterization strategies

To clearly observe the transition of microstructure and hardness from the weld interface zone (WZ) to base metal (BM), the cross-sectional samples were extracted perpendicular to the welding direction from the welding joints, hot-mounted, ground with SiC paper down to 4000 grit size, polished to a 1-μm finish using the red diamond suspension and then etched with 4 vol% Nital solution. The cross-sectional morphologies and microstructure at different zones of the joints were captured by Leica M205A Stereo Microscope and Leica MMRM light optical microscope (LOM), respectively. In-depth microscopic analysis was conducted using the JEOL JSM-7001F field emission gun scanning electron microscope (SEM) equipped with an electron backscatter diffraction (EBSD) detector with a magnification of ×250 and a step size of 0.9 μm. The obtained data

Table 1 Chemical composition of 440CL HSLA steel (wt%)

Steel	C	Mn	Si	Al	Cr	Ti	P	S	Nb	N	Fe
440CL	0.08	1.188	0.06	0.025	0.017	0.017	0.014	0.009	0.007	0.005	Bal

Fig. 2 **a** Gleeble 3500 thermo-mechanical test simulator, and **b** sketch map shows the assembling relation between specimens and clamps



was post-analysed by HKL Channel 5 software. The microhardness profiles were acquired by the Matsuzawa Via-F automatic Vickers Hardness Tester. The room-temperature tensile properties were evaluated through the Instron 8804 machine with a strain rate of 1 mm/min and a loading direction perpendicular to the weld direction. Whereafter, the fracture modes were determined by SEM.

3 Results and discussion

3.1 FBW thermal and mechanical histories

Figure 3 displays the weld thermal and mechanical cycle curves measured by thermocouples on conditions of varying δ_f and v_f values. By comparing the thermal history at varied δ_f and v_f (Fig. 3a, b), the high-temperature duration prolonged from 6.217 to 12.217 s as increased δ_f from 6 to 12 mm while the high-temperature duration narrowed from 10.217 to 1.328 s with accelerated v_f from 1 to 9 mm/s. As the distance between the measuring point and the contact surface is constantly shortened with the advance of the flash stage, and the temperature is controlled through the measuring point in this experiment, the actual temperature of the

contact surface will continue to rise with the increase of the flash time, indicating that a larger δ_f or a slower v_f may generate more heat input during the welding process. By comparison with the force–time profiles in different δ_f and v_f situations, samples with larger δ_f will bear axial pressure for longer (Fig. 3c) while samples applied with higher v_f will be subject to higher axial pressure with a shorter duration (Fig. 3d). An increase in δ_f contributes to the broadening in the width of the plastic zone which also implies the intensified heat input while an acceleration in v_f will shrink the heating zone and increases the difficulty of plastic deformation [25].

3.2 Macro morphologies of FBW joints

Figure 4 captured the representative macrographs of samples after FBW on conditions of various δ_f and v_f values. Distinctly extruded metal with burrs is carried on the contact face. Through comparing samples 1#~4#, it is clear that the overall length of welded specimens generally reduced with the increase of δ_f . Generally speaking, on the basis of guaranteeing decent welding formability and performance, the less the raw material loss, the smaller the theoretical and actual dimension deviation of the processed wheel rim. Therefore, a smaller δ_f will be preferred under the condition that the difference in welding performance was not obvious. According to the evolution of microstructural characteristics across the weld joint, 3 typical zones could be divided: WZ, coarse-grain heat affected zone (CGHAZ), and fine-grain heat affected zone (FGHAZ), as shown in Fig. 5a. No macro defect including cracks or pores could be detected across the weld joints implying the welding conditions are reliable [26]. Here, the WZ is too narrow to be accurately measured; therefore, the influence of flash parameters on the macrostructure was only compared via the width variation in HAZ. The extremely narrow WZ is formed by the retained liquid metal while the most liquid one splashed out of the contact surface during the flash stage. To make

Table 2 List of FBW parameters concerning the effect of flash allowance and speed

No.	Flash allowance (mm)	Flash speed (mm/s)	Upset allowance (mm)	Upset speed (mm/s)
1#	6	1	6.5	30
2#	8	1	6.5	30
3#	10	1	6.5	30
4#	12	1	6.5	30
5#	10	2.5	6.5	30
6#	10	5	6.5	30
7#	10	7	6.5	30
8#	10	9	6.5	30

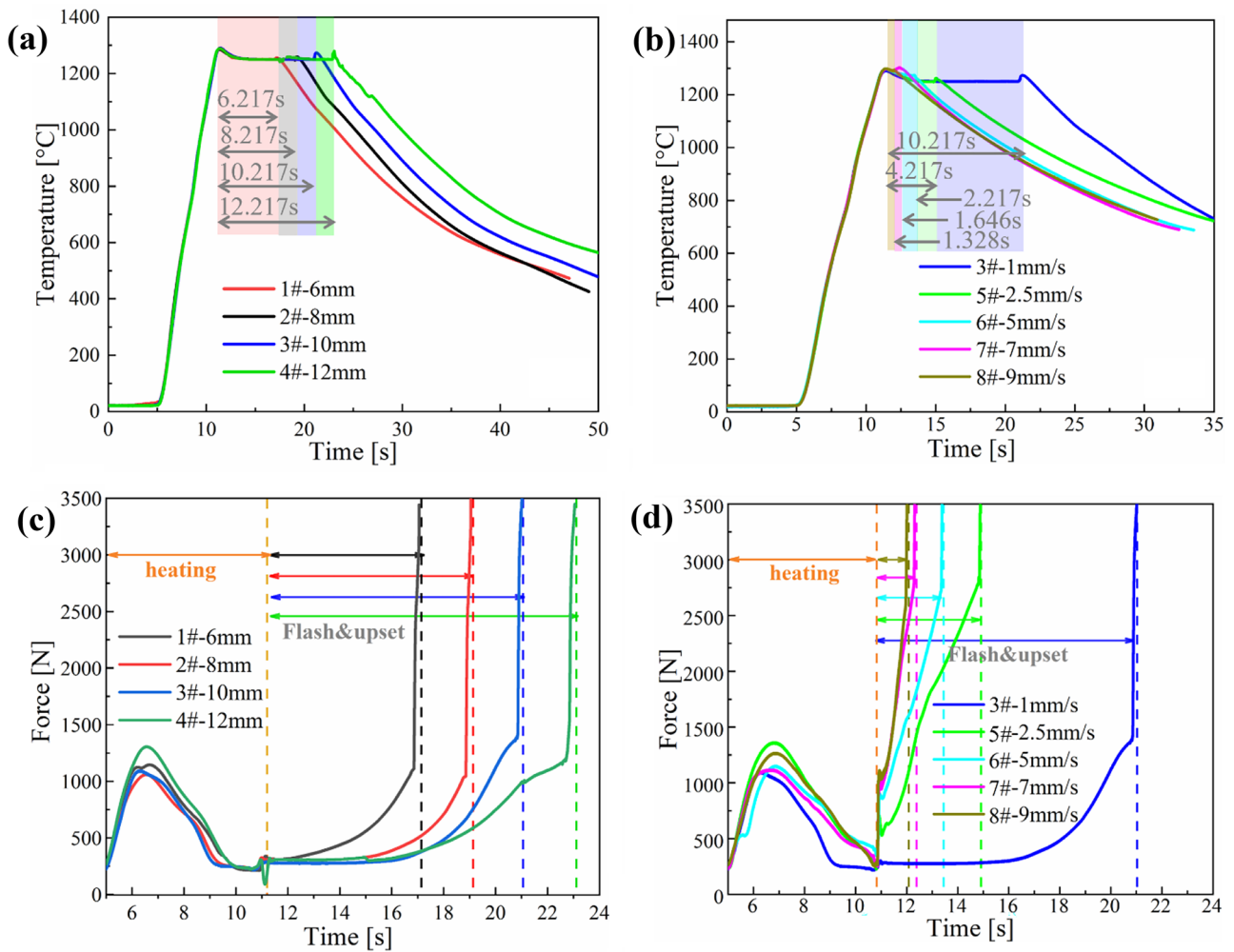


Fig. 3 Measurement profiles of the FBW thermal and mechanical cycles recorded at different flash allowances (a, c) and flash speeds (b, d)

the comparison more convincing, three positions including the upper surface, central and lower surface along the welding direction were checked. By measuring, the width

of CGHAZ and FGHAZ generally increased regardless of positions with increased δ_f , which is mainly related to larger heat inputs and grain coarsening (Fig. 5b). However,

Fig. 4 Representative macrographs of welds processed with different δ_f and v_f values

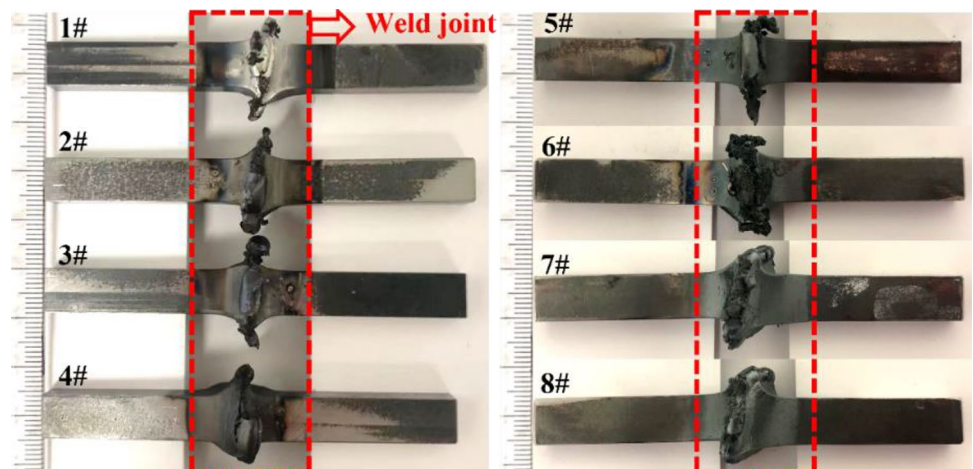
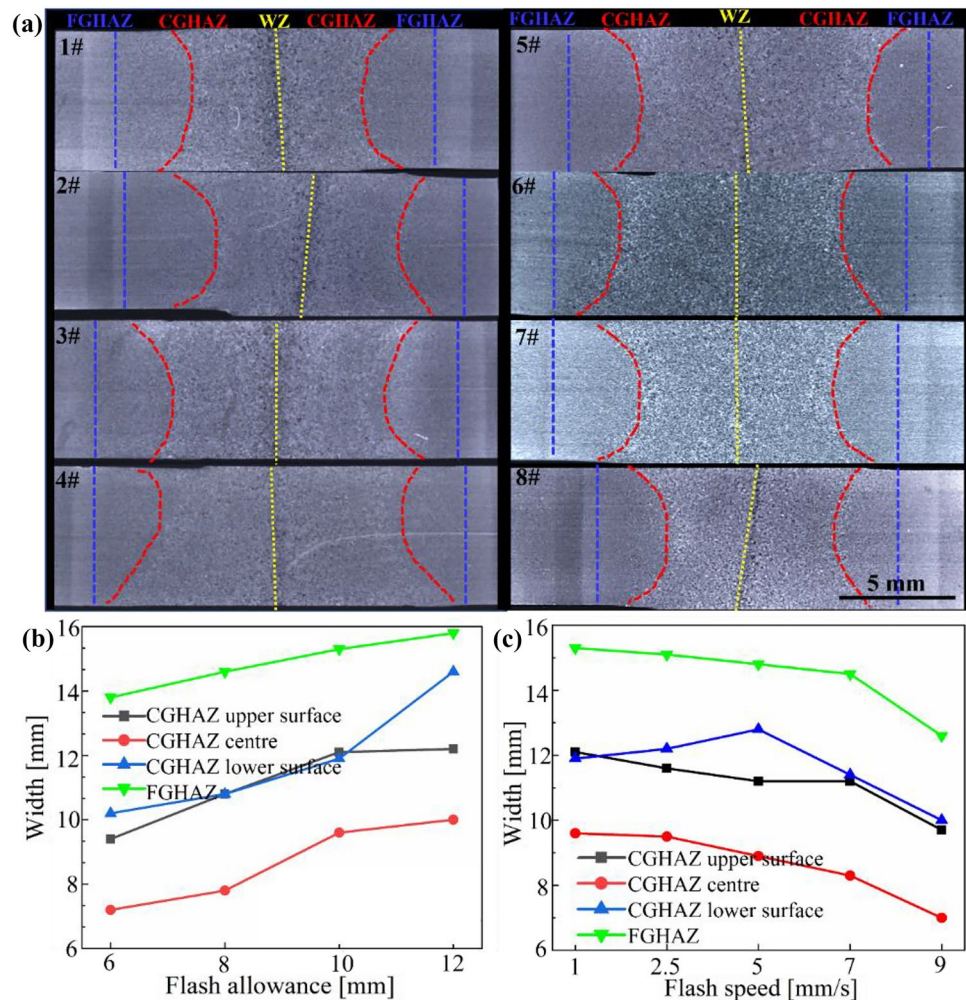


Fig. 5 Low-magnification microstructure of the seam welds in different parameter cases (**a** and **b**)



the width of CGHAZ and FGHAZ generally decreased as the v_f accelerated, due to the narrowed heating zone (Fig. 5c). δ_f represents the shortened length of the work-piece during the flash stage, which is positively correlated with the heat input. Under the appropriate δ_f , at the end of the flash stage, a liquid layer with a certain depth would be formed at the joint interface if an optimum δ_f is applied, possessing enough ability to bear plastic deformation and facilitate the following upset stage [20]. Besides, v_f has a reverse correlation with high-temperature duration and heat input but a positive correlation with plastic deformation. Therefore, only if an appropriate δ_f and v_f are applied, the joints would undergo moderate plastic deformation without significant grain coarsening, resulting in the minimum width of HAZ.

3.3 Microstructural evolution of FBW joints

To show the microstructural evolution across the weld joint more intuitively, light optical micrographs (LOM), grain

boundary misorientation angle distribution maps (GBMA) and geometrically necessary dislocations maps (GNDs) at WZ, CGHAZ and FGHAZ of specimen 1# are displayed in Fig. 6a–i. Low-angle grain boundaries (LAGBs) with a misorientation angle of $2^\circ \leq \theta < 15^\circ$ consist of an array of dislocations. A boundary misorientation lower than 2° is not considered due to the unreliable identification since the EBSD technique suffers from a lower angular resolution [27]. High-angle grain boundaries (HAGBs) with a misorientation angle of $\theta \geq 15^\circ$ could be viewed as an indicator showing the recrystallisation degree [28]. The formation of GNDs originates from the stored dislocations related to the non-uniform deformation, which creates a shear gradient giving rise to lattice rotation and net Burgers vector for sets of dislocations [29]. The mean GND density could be calculated from local average misorientation to further evaluate the stored energy. The corresponding grain size distribution, misorientation angle distribution and GND density distribution were further compared in Fig. 6j–l. The microstructure of WZ shown in Fig. 6a exhibited a

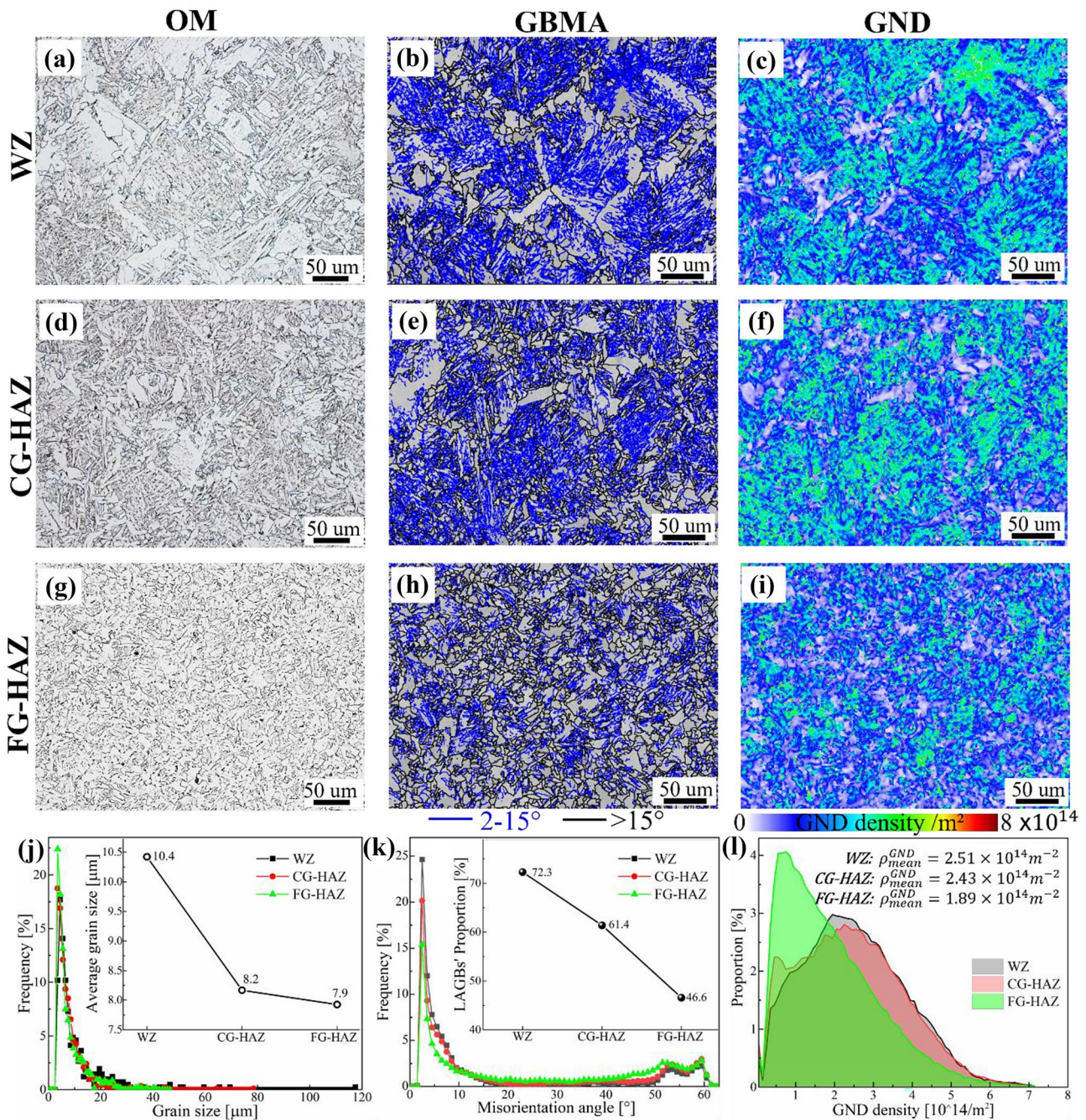


Fig. 6 Microstructural evolution across the 1# weld joint: light optical micrograph (LOM), grain boundary misorientation angle (GBMA) map and GND map taken at WZ are represented in (a), (b) and (c), respectively. LOM, GBMA and GND maps taken at CGHAZ are displayed in (d), (e) and (f), respectively. LOM, GBMA and GND

maps taken at FGHAZ are displayed in (g), (h) and (i), respectively. Comparisons of grain size distribution, GB angle distribution, and GND density distribution at three representative maps are exhibited in (j), (k) and (l), respectively

combination of various ferritic morphologies including acicular ferrite (AF), bainite ferrite (BF), and primary ferrite (PF), and Widmanstätten ferrite (WF) detectable. The local peak temperature in WZ was well above Ac3, leading to the BM being completely austenitized and transformed into PF via reconstructive transformation and other ferrites

via shear transformation. Compared to the PF with a typical equiaxed shape, the AF could be characterized by spiculate fine grains with multiple orientations while the BF usually possesses lath-like morphology. Concerning WF, it normally stems out from the grain boundary ferrite if the movement of the planar growth front slowed down [30].

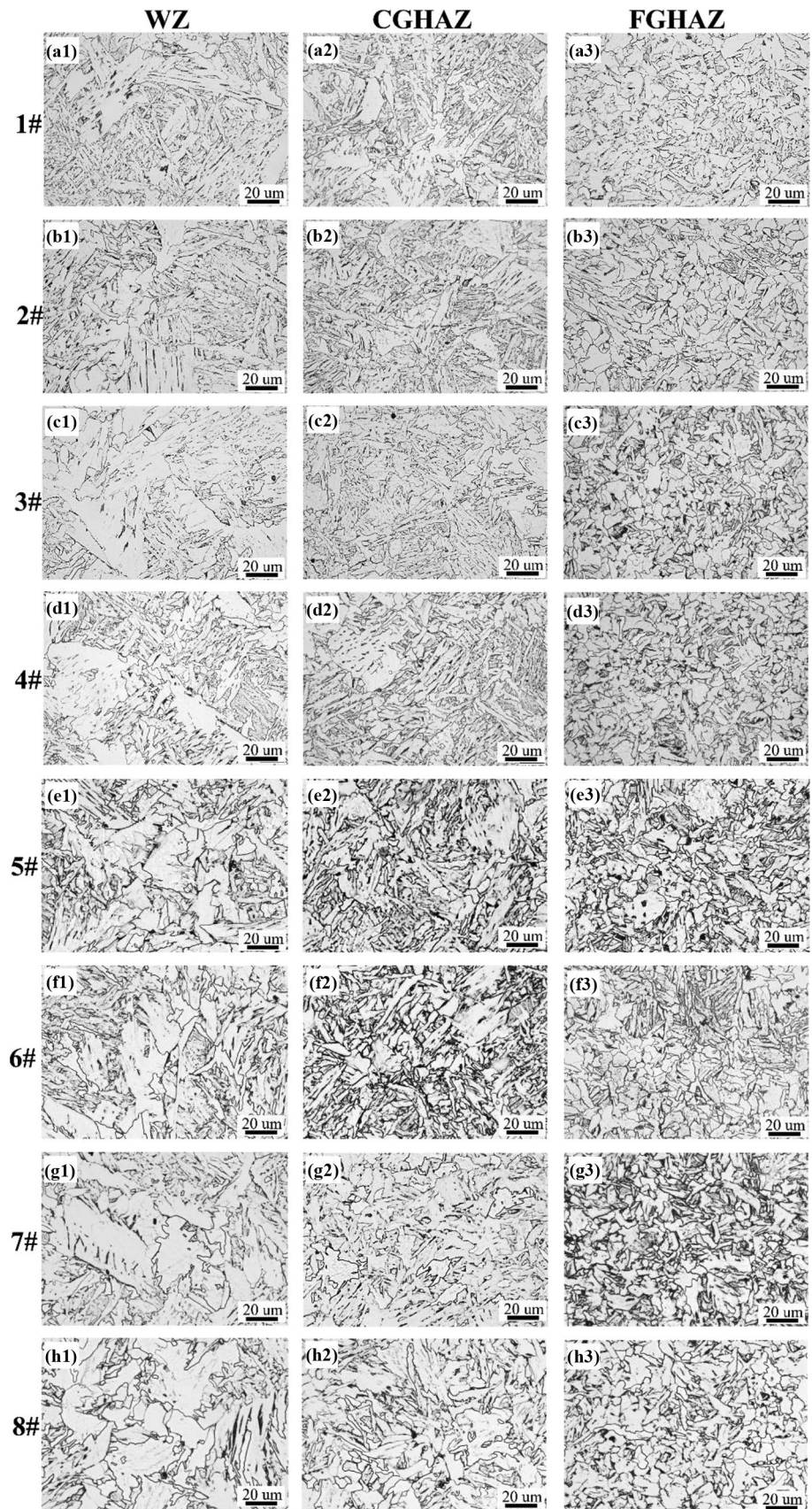
The GBMA map taken at WZ shown in Fig. 6b reveals that the LAGBs indicated by blue solid lines occupied a major proportion compared with the HAGBs indicated by black solid lines and are inclined to distribute in other ferrite grains except for PF. Similarly, higher GND density was found to spread over in AF, BF and WF compared with PF (Fig. 6c). This similarity can be attributed that the LAGBs are regarded as sequences of dislocations with certain orientations. A comparatively low GND density within PF grains is mainly because they had experienced fully recrystallized phase transformation at high temperatures with sluggish cooling rates [31, 32]. However, regions within PF grains at neighbourhood boundaries of other ferrite grains revealed slight GND densities. Such dislocations were generated and accumulated during the formation of AF, BF and WF with shape changes in the transformed zones [33]. Therefore, corresponding plastic deformation is induced in the PF to accommodate these geometrical changes, which causes the dislocation accumulation [34]. The microstructure of CGHAZ is quite similar to that of WZ but with more PF and a finer overall size of 8.2 μm compared with the grain size of 10.4 μm in WZ (Fig. 6d, j). Besides, the LAGBs' proportion in CGHAZ was calculated to be 61.4%, which is 10.9% smaller than that in WZ (Fig. 6e, k). Accordingly, the average GND density in CGHAZ was determined to be $2.43 \times 10^{14} \text{ m}^{-2}$, which is slightly lower than that of $2.51 \times 10^{14} \text{ m}^{-2}$ in WZ (Fig. 6f, l). This can be explained by a higher local peak temperature and severer plastic deformation taking place in WZ during the FBW process, leading to more dynamic recrystallization and dislocation accumulation in this area than in CGHAZ [9]. Also, during solidification, the molten material in WZ will be constrained between the contiguous solid counterpart that can hardly contract or expand, inducing the accumulation of thermal stresses and further the pile-up of dislocations [30]. By contrast, the FGHAZ show a considerable difference in microstructure, which consists of PF and a small quantity of AF and P with a further refined average grain size of 7.9 μm (Fig. 6g, j). In FGHAZ, the local peak temperature would be between A_{c1} and A_{c3} , so that only partial PF and P were austenitized and on cooling transformed to AF during FBW. Certainly, a relatively low local peak temperature in FGHAZ contributes to the refinement of grain size. It is clear from Fig. 6h, k and l and l that the LAGBs proportion and the average GND density both became smaller in FGHAZ when compared to the counterparts in WZ and CGHAZ, which is because the FGHAZ experienced minor plastic deformation during the FBW process [22].

To evaluate the effects of flash parameters on the microstructural evolution, the weld microstructures in WZ, CGHAZ and FGHAZ for different δ_f and v_f values are compared in Fig. 7. Overall speaking, the variation in flash

parameters exerts little influence on the microstructure constitution: WZ mainly consisted of a typical coarse solidification structure including AF, BF, PF and WF; the CGHAZ possesses similar microstructural composition with WZ but much finer; the FGHAZ is composed of refined PF, AF and P. On the contrary, the influence of flash parameters is mainly reflected in the proportion of different ferrite types and grain sizes. With the increase of δ_f , the area fraction of PF and WF increased while AF and BF decreased in WZ, as shown in Fig. 7a1–d1. Also, the same phenomenon occurs in the CGHAZ with the accumulation of δ_f , as shown in Fig. 7a2–d2. On the impact of flash speed, the content of PF increased while the fraction of AF, BF and WF decreased in WZ and CGHAZ with accelerated v_f , as shown in Fig. 7c1, e1–h1, c2, e2–h2, respectively. These microstructure evolutions in WZ and CGHAZ are highly influenced by the heat input and plastic deformation during the FBW process. The welding heat input is positively correlated with δ_f and negatively related to v_f . As the δ_f increases, the consequently increased high-temperature duration enables the prior austenite (PA) grains to grow up and coarsen. When the FBW samples cooled below A_{c3} , proeutectoid ferrite nucleates at PA grain boundaries and grows into reticular allotriomorphic ferrite since the growth rate of ferrite along the PA grain boundary is much faster than inwards, and with the longer high-temperature duration, the proeutectoid ferrite gradually increases and widens, and then transformed into massive PF within PA grains. Although a larger v_f would result in a smaller heat input, a severer plastic deformation would be arisen during high temperature, leading to the aggravation of dynamic recrystallization and thus promoting the nucleation and growth of PF [31]. Additionally, the transformation from PA to WF is principally a displacive transformation with the carbon diffusion-controlled growth rate [35]. A higher heat input encouraged by longer δ_f or lower v_f in the welding process will be more beneficial to the carbon diffusion, thus the WF will be more in favour of nucleating and growing up from the resulted coarse PA [36]. Furthermore, the AF proportion in FGHAZ mildly increased with increased δ_f (Fig. 7a3–d3) while gradually decreasing with increased v_f and nearly disappeared when the v_f exceeds 7 mm/s (Fig. 7c3, e3–h3). This is because high heat input induced by large δ_f or low v_f will increase the local peak temperature, leading to more proportion of PF and P from BM being austenitized and then transformed into AF. Therefore, it is more likely that the local peak temperature at FGHAZ is too close to A_{c3} to enable the nucleation of AF to transform from the parent microstructure once the v_f is faster than 7 mm/s.

To further investigate the effects of flash parameters on the grain morphology, distributions of misorientation angle and dislocation density, EBSD was performed on WZ and CGHAZ of the welded samples processed with

Fig. 7 LOM images in WZ, CGHAZ and FGHAZ of samples processed with different flash parameters: **a1–a3** sample 1#; **b1–b3** sample 2#; **c1–c3** sample 3#; **d1–d3** sample 4#; **e1–e3** sample 5#; **f1–f3** sample 6#; **g1–g3** sample 7#; **h1–h3** sample 8#



varied δ_f and v_f values, as shown in Figs. 8 and 9. Need to note, all the EBSD maps taken at CGHAZ were scanned at the same distance from the weld line. According to the image analysis obtained by these EBSD maps, comparisons on grain size, misorientation angle transition and GND density of samples with different parameters are presented in Fig. 10.

By comparing the IPF maps and GB maps taken at WZ of welded samples 1#, 3# and 4# shown in Fig. 8a, b, d, e, h, g), it can be speculated that the irregularly polygonal-shaped grains without dense transgranular LAGBs represent PF and became coarser with a smaller aspect ratio as increased δ_f . Besides, the grain clusters with densely distributed LAGBs interiorly refer to AF, BF or WF, and their

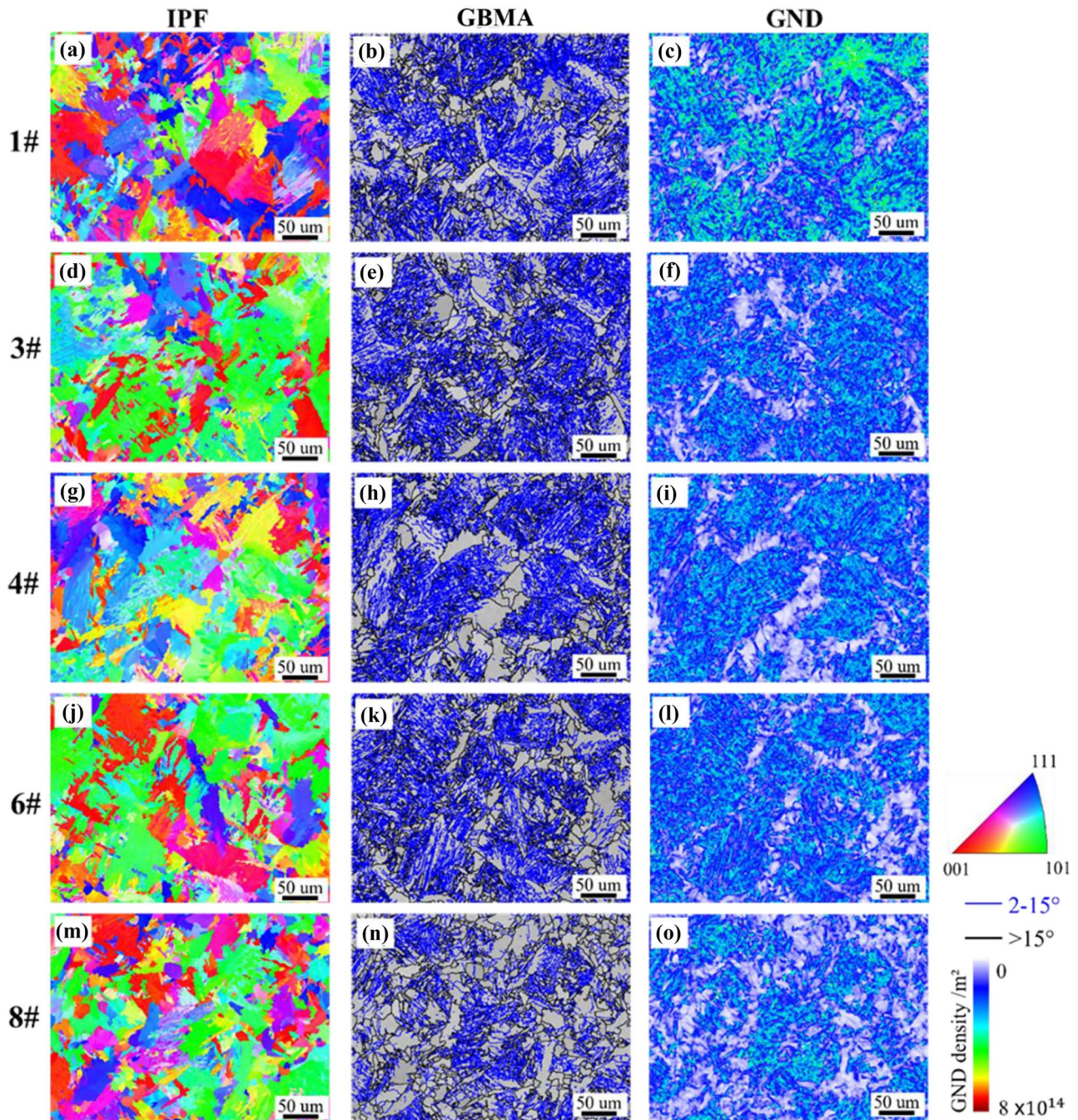


Fig. 8 EBSD analysis including inverse pole figure (IPF) maps, misorientation angle distribution maps, and GND density distribution maps taken at WZ of samples processed with different flash param-

eters: **a–c** 1#; **d–f** 3#; **g–i** 4#; **j–l** 6#; **m–o** 8#. The crystal orientation-colour relation map corresponds to the colour-coded stereographic triangle IPF

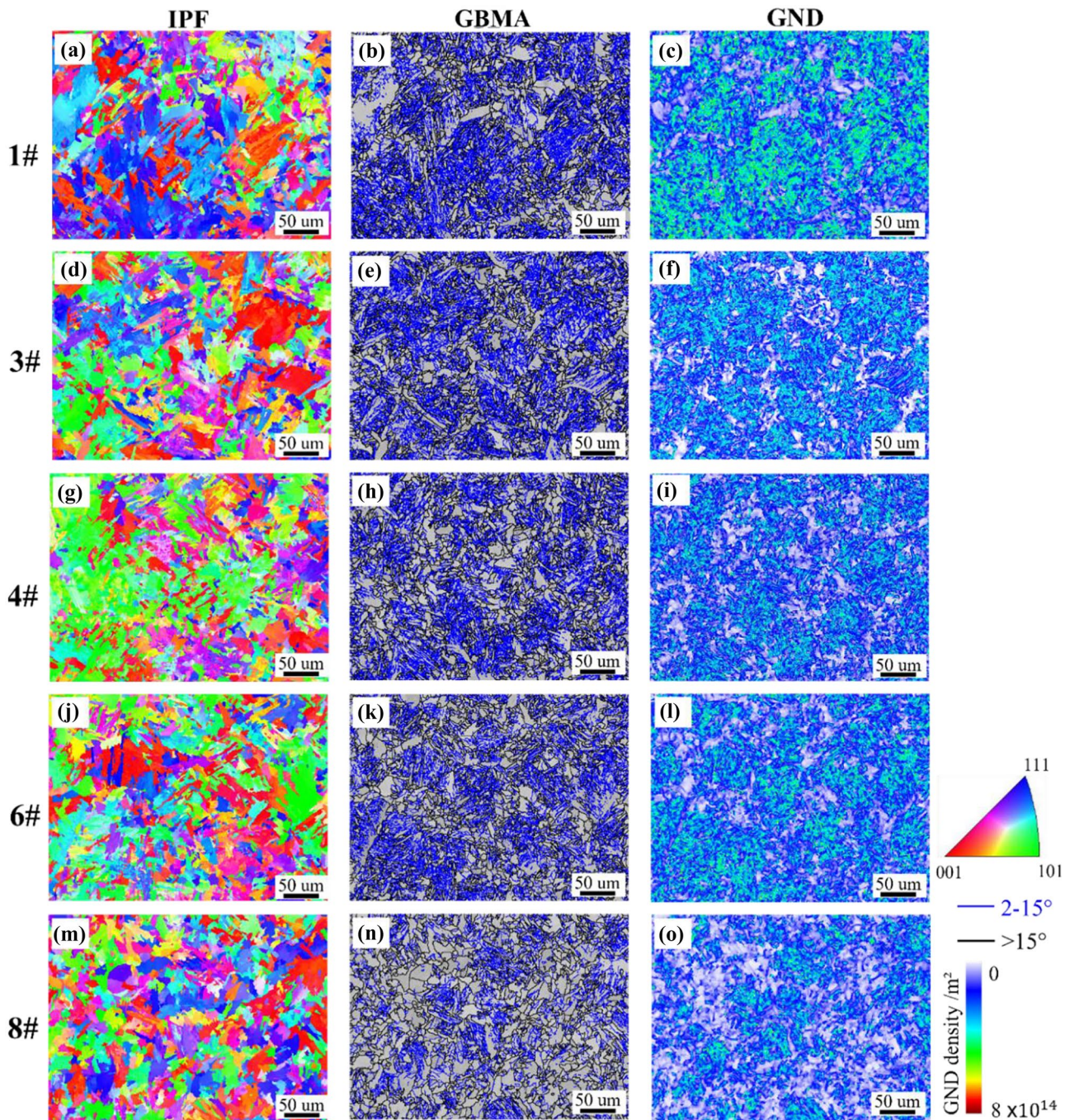


Fig. 9 EBSD analysis including IPF maps, misorientation angle maps and GND density distribution maps taken at CGHAZ of samples processed with different flash parameters: **a–c** 1#, **d–f** 3#, **g–i** 4#, **j–l** 6#, **m–o** 8#

proportion decreased slightly with the increase of δ_f . Likewise, the GND density was found higher within these grain clusters and became smaller over δ_f , as implied in Fig. 8c, f, i. According to the variation in grain size quantitatively plotted in Fig. 10a, the mean grain size in WZ underwent a mild down-and-up trend with the accumulation of δ_f , showing a negative correlation with the proportion of fine grains

(< 10 μm). Furthermore, the overall LAGBs' fraction and GND density in WZ slightly reduced with the increment of δ_f statistically indicated by Fig. 10c, e, respectively. It is known that the co-presence of high temperature and severe strain during FBW will compel the weld joints to experience dynamic recrystallization [37]. The recrystallization processing level would be intensified when applying a higher

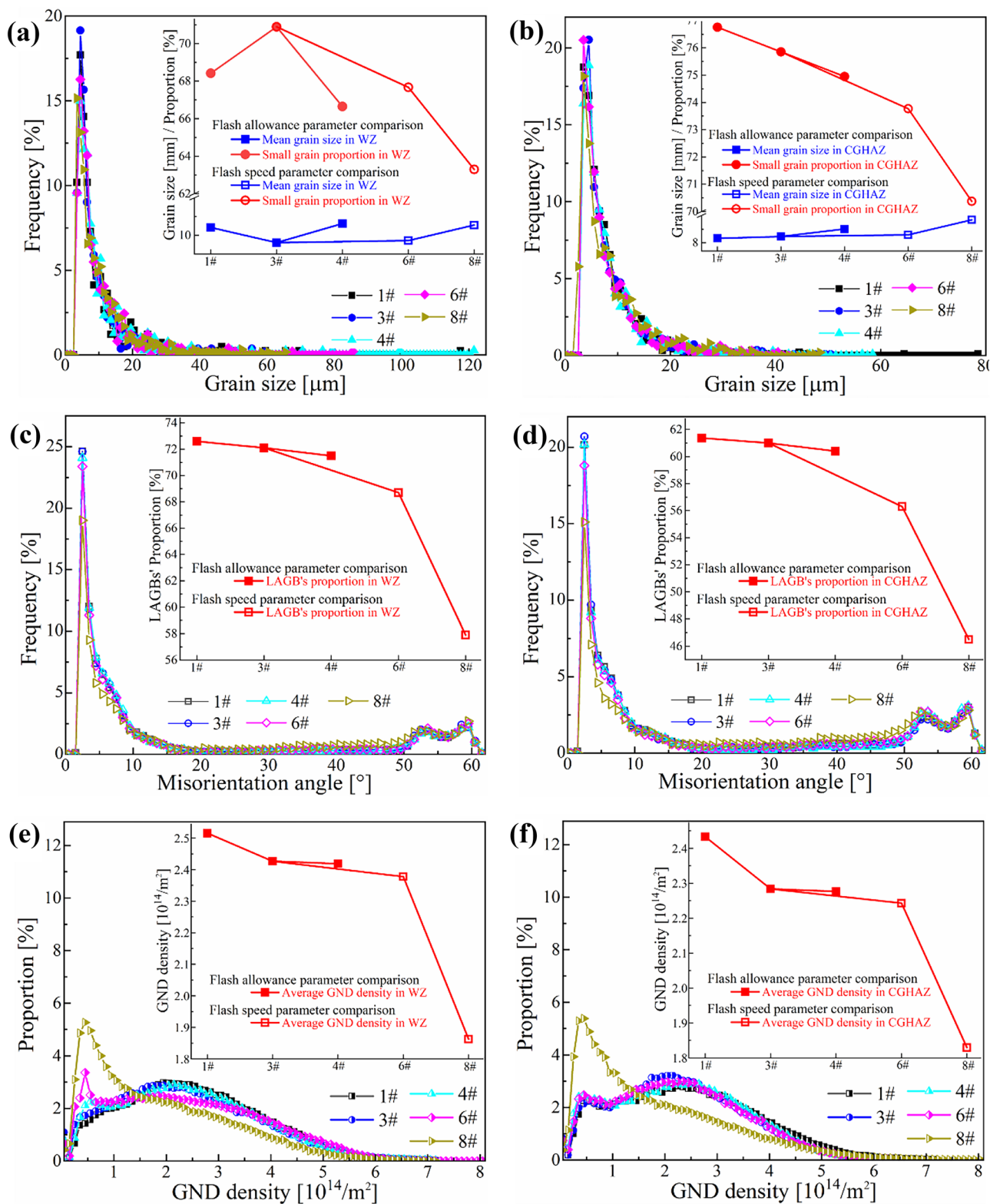


Fig. 10 Comparison of the effects of flash parameters on the grain size distribution (a, b), misorientation angle distribution (c, d) and average GND density (e, f)

heat input which could be caused by increased δ_f , leading to the increase in the fraction of HAGBs and the decrease in dislocation density. A comparatively smaller average grain size detected in WZ of sample 3# ($\delta_f=10$ mm) could give the credit to less extra coarse grain fraction that stemmed from the further homogeneous growth of the recrystallized grains.

Meanwhile, the acceleration in v_f populated the WZ with more homogeneous grains accompanied by a smaller aspect ratio, more HAGBs distributed and lower dislocation density, as indicated by samples 3#, 6# and 8# shown Fig. 8d–f, j–l, m–o, respectively. Especially when the v_f speeds up to 9 mm/s (sample 8#), the majority of the grains are near equiaxed and the LAGBs are no longer dominant obviously. According to the grain statistics shown in Fig. 10a, the average grain size showed up an upward trend while the small grain proportion greatly dropped by around 8% when the v_f was added to 9 mm/s. The LAGBs' fraction sharply reduced from 72 to 58% and the GND density declined from $2.42 \times 10^{14}/\text{m}^2$ to $1.85 \times 10^{14}/\text{m}^2$ as the v_f increased from 1 to 9 mm/s, as shown in Fig. 10c, e, respectively. It has been reported that a decrease in PA grain size induced by lower heat input may budge the CCT curve towards shorter cooling duration and higher temperature to favour the transformation of PF [31]. Therefore, more PF transformed at WZ during solidification with faster v_f causes these microstructural trends.

Since CGHAZ is just adjacent to WZ, the comparatively lower local peak temperature and slower cooling rate still caused the evolution of various ferrites with a finer size similar to those in WZ, as shown in Fig. 9. The mean grain size exhibited an upward trend, while the small grain proportion showed a downward tendency with the advancement of δ_f , as reflected by Fig. 9a, d, g and the corresponding statistics in Fig. 10b. This is because a higher heat input would arise at larger δ_f that will be in favour of grain coarsening. Likewise, a similar trend in the average grain size and fine grain fraction with the acceleration of v_f was observed, as shown in Figs. 9d, j, m and 10b. Generally, a smaller heat input will be generated at a faster v_f , which would be supposed to refine grain size. However, the acquired microstructure at higher v_f showed more presence of PF confirming a shrunken heating zone overrode other factors in affecting the final microstructure and average size. The fraction of LAGBs experienced a continuous reduction both with the increase of δ_f and v_f , as shown in Figs. 9b, e, h, k, n and 10d. Furthermore, the variation of GND density showed a similar tendency as the LAGBs' proportion with the increment of δ_f and v_f , as indicated in Figs. 9c, f, i, l, o and 10f. These tendencies can be explained by the increased volume fraction of the fully recrystallized PF phase with quite a low dislocation density.

Generally speaking, the heat input increases with an increase in δ_f and a decrease in v_f . An appropriate δ_f should

guarantee that a molten metal layer formed on the end face of the whole workpiece at the end of the flash stage and the plastic deformation temperature could be achieved at a certain depth. If excessively small δ_f could not meet the above requirements, therefore, the welding quality will be affected. Exaggerated δ_f will cause a waste of raw materials and a reduction in productivity. An optimum v_f should be fast enough to ensure the intensity and stability of the flash. However, if the v_f is too large, the heating zone will be too narrow, which will increase the difficulty of plastic deformation. Meanwhile, the welding current will be increased in that circumstance, leading to an increase in the nozzle depth after lint beam blasting, and the deterioration of the weld joint quality. Hence, an optimum heat input could achieve sufficient metal flow and adequate plastic deformation, consequently, contributing to a defect-free weld joint. Moreover, the optimum heat input could produce a fine recrystallized grain structure accompanied by sufficient dislocation density to ensure an optimal match of strength and plasticity [38].

3.4 Microhardness transition across FBW joints

The variation in microhardness transition at the upper, central and bottom of the plate thickness across the weld line regarding different flash parameters is plotted in Fig. 11a–h. From the hardness transition profiles, it can be observed that the microhardness trendline is roughly symmetric and similar at different parameters: the microhardness value reached the maximum at or near the WZ and then decreased toward the base metal (~ 150 HV). The hardness is higher in HAZ than BM except for a slightly low ebb observed at the transition zone to BM at sample 8# with a v_f of 9 mm/s. For the rest, the softening phenomenon was not detected in the HAZ of samples processed with other parameters. According to the comparison of microhardness transitions over δ_f shown in Fig. 11i, the hardness value of WZ is around 202 HV at $\delta_f=6$ mm and slightly reduced to 195 HV when δ_f reached 12 mm, which is 1.3–1.35 times harder than that of BM. The hardness in WZ slightly decreased with the increment of v_f from 1 to 5 mm/s. Whereafter, a steep drop has been seen in the hardness value of WZ from 192 to 177 HV when the v_f speeds up from 5 to 9 mm/s, as can be seen in Fig. 11j. Several factors exert an essential role in contributing to the hardening of WZ, including strain localization, substructure and phase transformation [30, 39]. The strain localization induced by residual stresses and microstructural heterogeneity generated during the FBW process would be conducive to the increase in hardness. The accumulation in substructure boundaries will also contribute to obstructing the movement of dislocations, therefore, would be attributable to the improvement in hardness [33]. Furthermore, the ferrite transformation including the development of

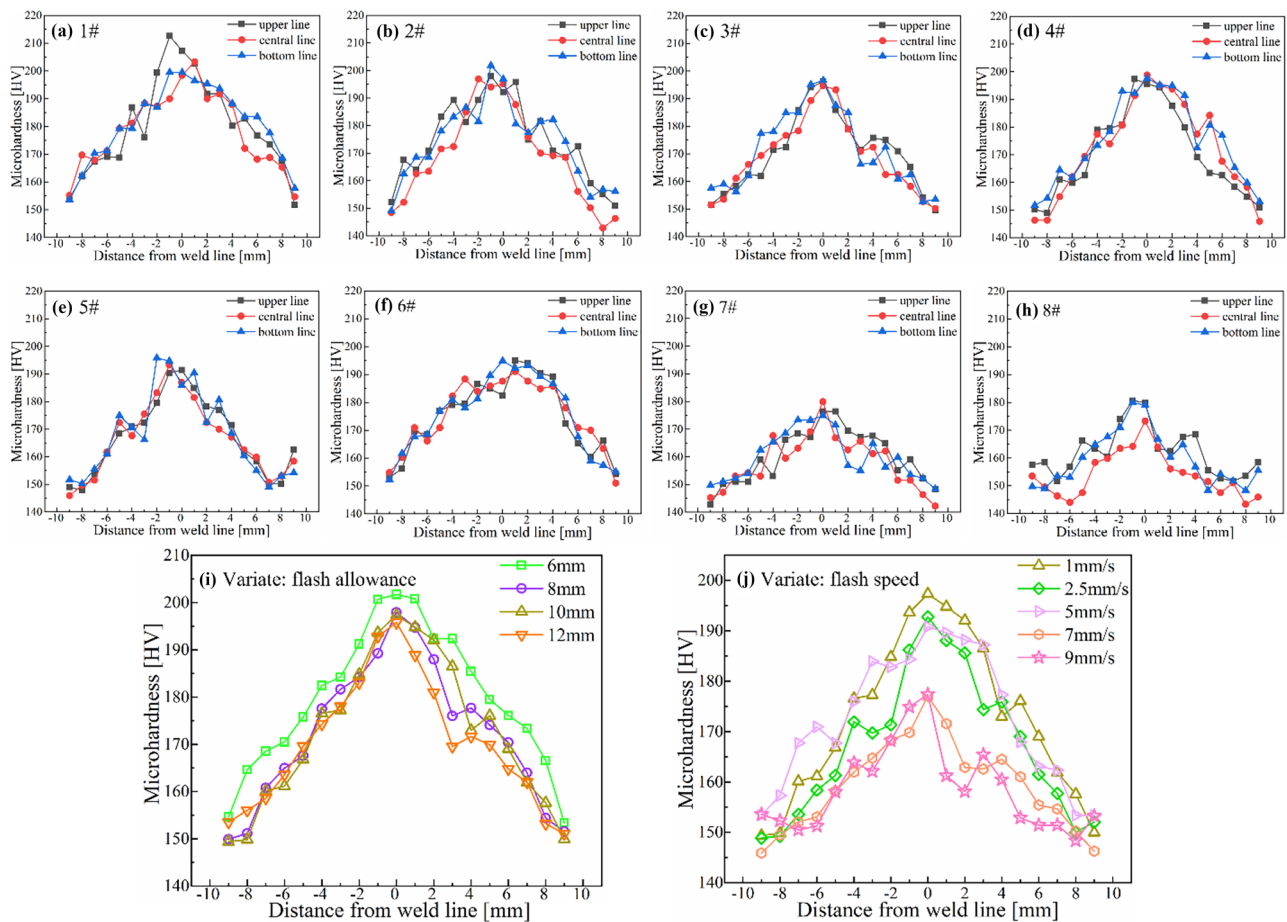


Fig. 11 Microhardness transitions across the weld line regarding different flash parameters: **a–h** comparisons on the microhardness transition on the weld joints processed with different δ_f and v_f values (**i–j**)

AF and BF is highly correlated to the hardness variation. Compared to the PF which is normally viewed as a fully recrystallized phase, AF mostly nucleates at deformed PA and is known to be an ideal structure with high strength and good toughness assured [40]. The BF that transformed at lower temperatures and faster cooling rates is known to have higher dislocation density and hardness than PF as well. Therefore, an increase in δ_f would enable more high-temperature duration to promote a dynamic recrystallization process that causes the reduction in AF and BF fraction in the fusion region and further results in hardness declining of WZ. However, an over acceleration in v_f will narrow the heating zone and increase the difficulty of plastic deformation, thus confining the nucleation of AF and BF to achieve a decrease in hardness.

3.5 Tensile properties of the FBW joints

Figure 12a, d display the strain–stress curves of welded joints processed with different δ_f and v_f that were gained from the

ambient uniaxial monotonic tensile tests. In the elastic strain stage, the slope of the strain–stress curves showed little variation indicating there is no obvious difference in stiffness as the flash parameter changes. The yield point is noticeable for all welding conditions due to the nitrogen and carbon interstitial atoms pinning/unpinning dislocations [41]. Besides, in the plastic strain stage, obvious changes in strain–stress behaviour could be observed that specimens start yielding at lower strains with the increase of δ_f and v_f . To better reveal the influence of flash parameters on the variation in plasticity and strength, the plasticity including elongation (EL) and area of reduction (RA) and the strength including yield strength (YS) and ultimate tensile strength (UTS) for the different FBW conditions were obtained and compared in Fig. 12b, c, e, f). For better comparison, the tensile properties of the material in as-received status were also detected using the same strain rate, and the EL, RA, YS and UTS were determined to be 45%, 79%, 362 and 466 MPa, respectively. The tensile properties of FBW joints exhibit a good match with those of BM, with a slight increase in strength (UTS:

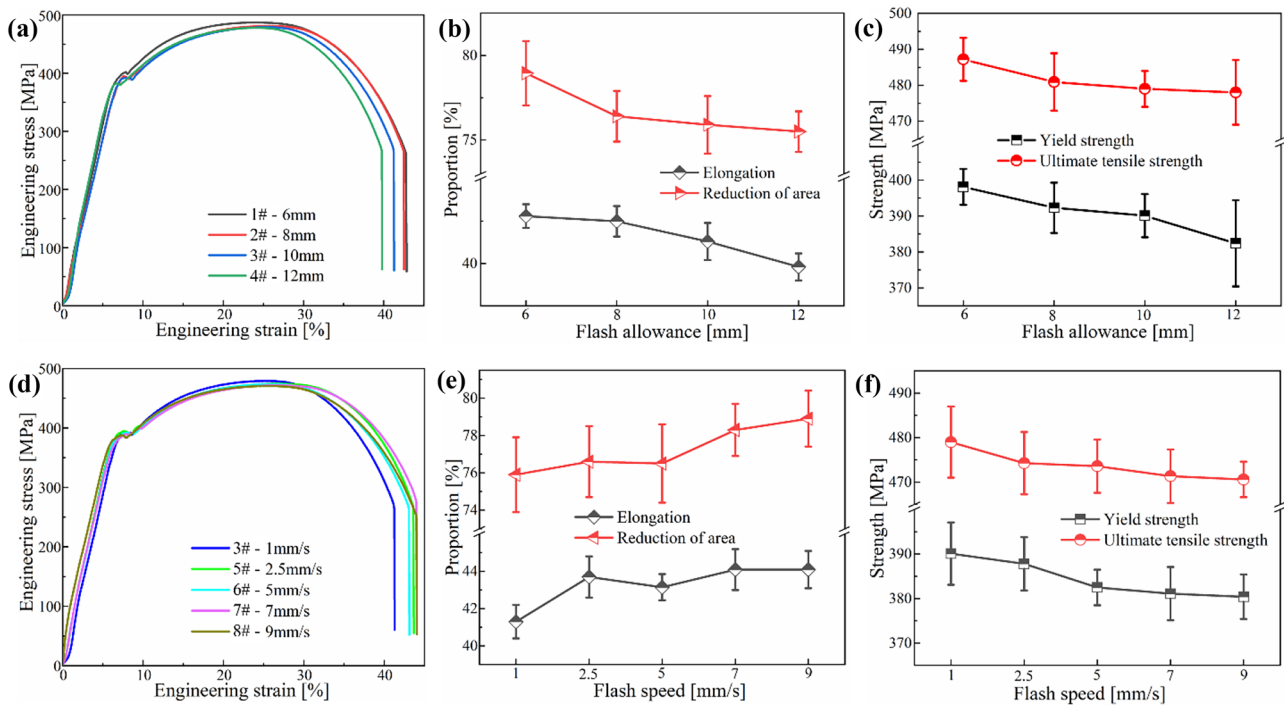


Fig. 12 Room-temperature tensile engineering strain–stress curves (a), corresponding ductility (b) and strength results (c) of the FBW joints processed with different δ_f ; ambient tensile engineering strain–

stress curves (e), corresponding ductility (d) and strength results (f) of the FBW joints processed with different v_f

468 ~ 493 MPa; YS: 370 ~ 403 MPa) but a mild decrease in plasticity (EL: 39 ~ 44%; RA: 74 ~ 79%). The reduction in ductility could be explained by a local compromise resulting from the strain localization due to the microstructural heterogeneity and residual stress induced by FBW. Furthermore, both the joint strength and ductility showed a downward tendency with the increment of δ_f , which could ultimately attribute to higher heat input. Increasing quantities of WF will nucleate while the transformation of fine AF and BF will be further inhibited when the heat input is excessive, resulting in the mild degradation of strength and plasticity simultaneously. Furthermore, according to the grain refinement strengthening and dislocation strengthening mechanisms, finer average grain size and smaller dislocation density obtained by increased δ_f would also contribute to the enhancement in strength [42]. However, the strength slightly decreased while the plasticity increased with the advancement of v_f . This is because less AF/BF with high dislocation density will be generated but more PF will nucleate under the circumstance of lower v_f due to the narrowed heating region during FBW, causing a decrease in strength but an increase in plasticity. Even though the mean grain diameter was refined with the acceleration in v_f , the recrystallization softening degree and decrease in dislocation density would be fostered, leading to the tendency for improved plasticity at a slight sacrifice of strength.

After tensile tests, the microstructure of three sites (A, B, C) outward from the fracture zone of all specimens is checked and shown in Fig. 13a–h. The microstructure in site A for all samples was determined to be composed of PF, AF and P, which is the typical microstructure of FGAZ. The microstructure in site B mainly consists of PF and P with insignificant deformation, belonging to the BM part. However, the PF and P grains near the fracture (site C) are severely stretched in the tension direction, where cracks are initiated and propagated along the austenite grain boundaries and possess an obvious directionality under axial stress. Even though a great extent of necking took place by HAZ, it still can be found that all tensile samples were fractured at the BM location. This is reasonable and can be explained from two aspects. On one hand, the basic microstructures of BM are PF and P while the welding zone mainly consists of BF and AF, and the strength of BF and AF is better than that of PF and pearlite, leading to strengthening and premature failure of the joints. On the other hand, the welding zone was formed suffering severe plastic deformation and subsequent recrystallization process; therefore, the deformation ability is superior to that of BM.

The fracture surface morphologies of tensile specimens processed with different flash parameters are displayed in Fig. 14a–h. It can be found that the parabolic and equiaxed dimples with different sizes and depths were the main

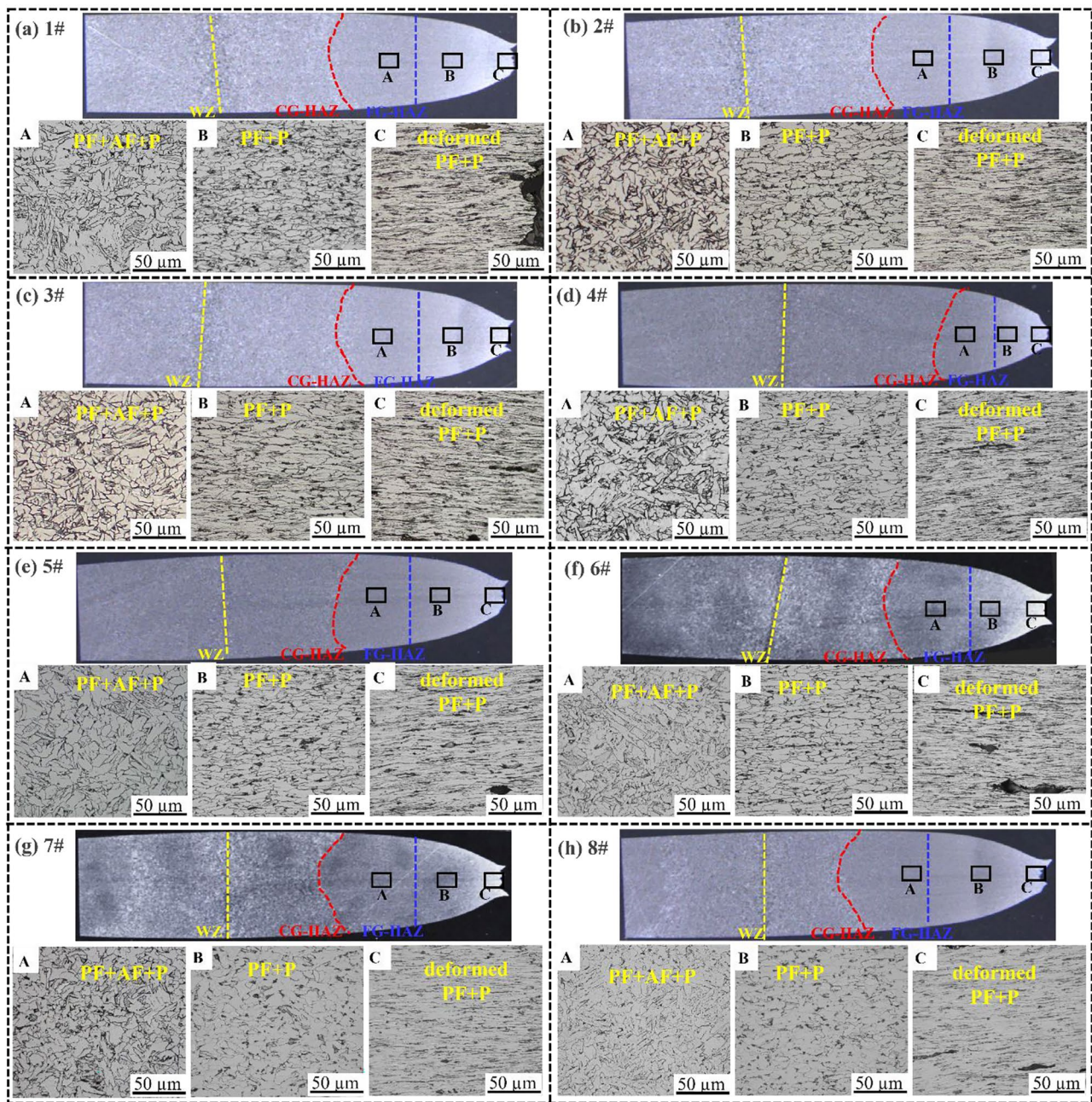


Fig. 13 Microstructure observation near to far from fracture location A–C at the fractured tensile specimens processed with different flash parameters: **a** 1#; **b** 2#; **c** 3#; **d** 4#; **e** 5#; **f** 6#; **g** 7#; **h** 8#

feature in all welding conditions, which could be characterized as a typical ductile fracture. Some extent of tear marks could also be seen on the boundaries of dimples, indicating the occurrence of exaggerated plastic deformation during the FBW process [21]. Besides, several spherical inclusions could be observed at the base of some large and deep dimples. The EDS map and point checking displayed in Fig. 14i show that these inclusions are rich in Mn, Ca, S, Al and O, which could be inferred as MnS, CaS and Al_2O_3 .

The fracture mechanism is highly correlated to the different expansion modes of the microvoids that existed in the welded joints during the tension process. Due to the local plastic deformation, micro-cracks initiated and propagated at the interface of the second-phase particles, namely the inclusions. Thereafter an internal shrinkage neck is generated in the local micro-region between the inclusion and the matrix. When the neck reaches a certain extent, it will suffer tear or shear fracture that forms the dimple fracture

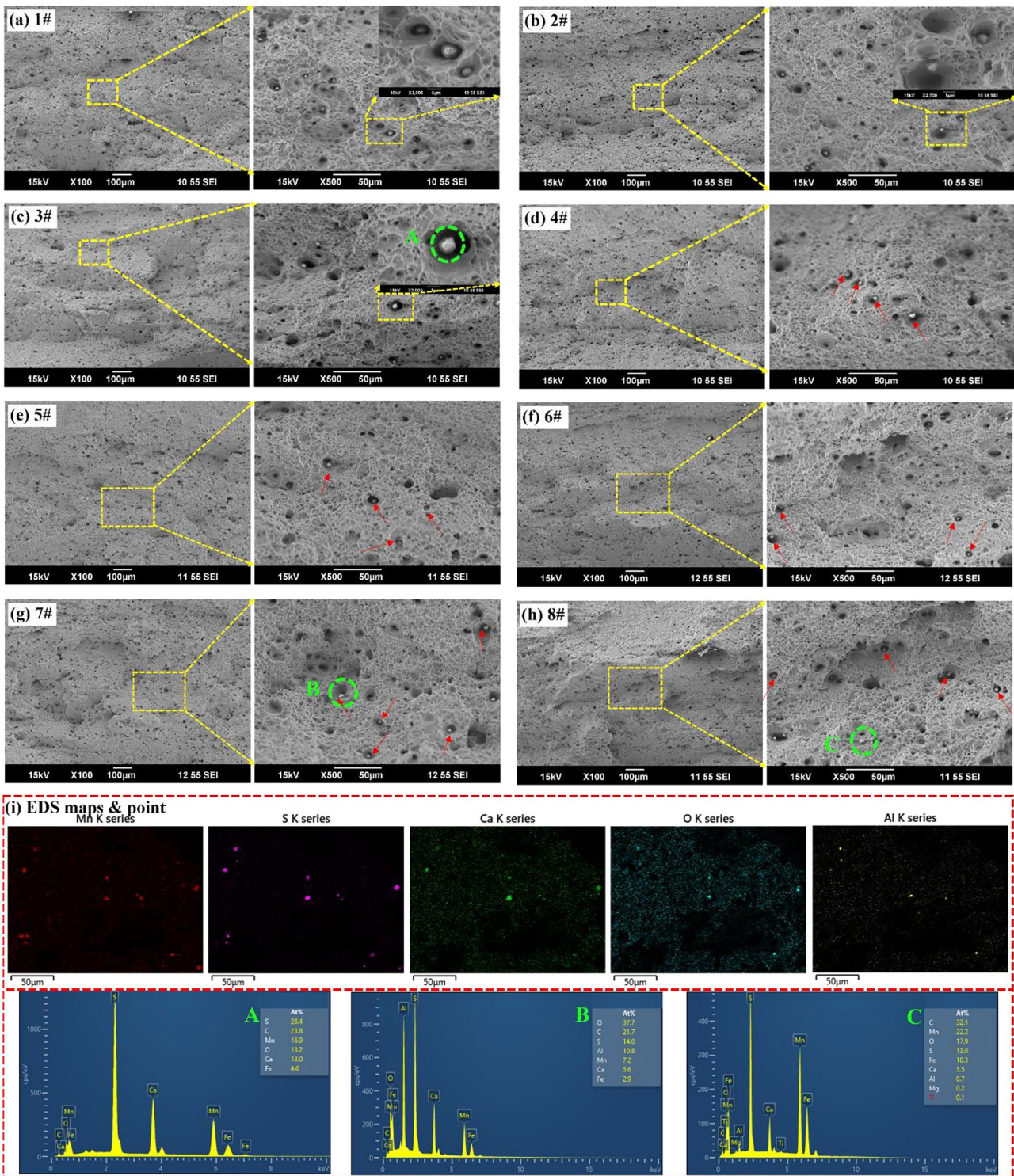


Fig. 14 Fracture morphologies taken at different magnifications (100× and 500×) of tensile specimens processed with different flash parameters: **a** 1#; **b** 2#; **c** 3#; **d** 4#; **e** 5#; **f** 6#; **g** 7#; **h** 8#; **i** EDS map-

ping results correspond to Fig. 14c at the magnification of 500× and EDS point results correspond to locations A, B and C

morphology. According to different stress states, dimples can be divided into orthogonal fracture dimples and shear fracture dimples. Under the action of normal stress that is

evenly distributed on the whole surface of the fracture, the micropores perpendicular to the principal stress grow up evenly in all directions and finally form equiaxed dimples

with small plastic deformation. Nevertheless, the shear and tear stress, compel the micropores to bear uneven stress during nucleation and growth, resulting in the formation of parabolic dimples and increasing the plastic deformation. As can be seen from Fig. 14, the tensile fracture of welded joints under different flash parameters contains parabolic dimples, equiaxed dimples and tearing edges, indicating the fracture mechanism refers to a mixed ductile fracture of normal fracture and shear fracture.

4 Conclusions

In this investigation, the FBW process of 440CL HSLA steels was physically simulated and the influence of flash parameters including δ_f and v_f on the microstructure evolution and mechanical performance of FBW joints was systematically analysed. The following conclusions could be summarised.

1. The CGHAZ showed similar ferritic morphology to WZ but with more PF and a finer average size. The FGHAZ showed considerable difference in microstructure, consisting of further refined PF and minor AF and P. The highest LAGBs' proportion and GND density were found in WZ in comparison with HAZs resulting from a higher local peak temperature and severer plastic deformation taking place in WZ.
2. The width of CGHAZ and FGHAZ generally increased with increased δ_f due to higher heat input and declined with the accelerated v_f due to the narrowed heating zone. The fraction of PF and WF increased while AF and BF decreased in WZ and CGHAZ as increased δ_f . With the acceleration of v_f , the PF content increased while the fraction of AF, BF and WF decreased in WZ and CGHAZ. The mean grain size in CGHAZ exhibited an upward trend while the LAGBs fraction and GND density experienced a continuous reduction with the advancement of δ_f and v_f .
3. The microhardness value reached the maximum at or near the WZ and then decreased toward the base metal (~150 HV). The hardness in WZ reduced from 202 to 195 HV when the δ_f increased from 6 to 12 mm. A steep drop has been seen in the hardness value of WZ from 192 to 177 HV when the v_f speeds up from 5 to 9 mm/s. All tensile samples were fractured at the BM location and the tensile properties of FBW joints exhibit a good match with those of BM, with a slight increase in strength (UTS: 468~493 MPa; YS: 370~403 MPa), but a mild decrease in plasticity (EL: 39~44%; RA: 74~79%). Furthermore, both the joint strength and ductility showed a downward tendency with the increment of δ_f . However, the UTS and YS slightly decreased

while the EL and RA increased with the advancement of v_f . The fracture mechanism refers to a mixed ductile fracture of normal fracture and shear fracture.

These findings are of great guiding significance in providing an appropriate process window concerning real production in FBW of HSLA steels with optimized microstructure and mechanical performance.

Acknowledgements This study was financially supported by the HBIS collaborative project (NO. IRIS-200506001), the University of Wollongong (UOW), and the Electron Microscopy Centre of UOW (EMC).

Author contribution JW: methodology, data curation, writing the original draft. YL: methodology, review and editing. JH: methodology. JQ: resources. LS: resources. ZJ: supervision, review and editing, project administration. CM: resources. VL: supervision, review and Editing, project administration.

Funding Open Access funding enabled and organized by CAUL and its Member Institutions.

Availability of data and material All data included in the current work are available upon request by contacting the corresponding author.

Declarations

Ethical approval The author obliged all the rules regarding the ethic in publication.

Consent to participate All the author's consent regarding the data provided in the text as well as the order of authorship.

Consent for publication All the authors consent regarding publication immediately after acceptance.

Competing interests The authors declare no competing interests.

Open Access This article is licensed under a Creative Commons Attribution 4.0 International License, which permits use, sharing, adaptation, distribution and reproduction in any medium or format, as long as you give appropriate credit to the original author(s) and the source, provide a link to the Creative Commons licence, and indicate if changes were made. The images or other third party material in this article are included in the article's Creative Commons licence, unless indicated otherwise in a credit line to the material. If material is not included in the article's Creative Commons licence and your intended use is not permitted by statutory regulation or exceeds the permitted use, you will need to obtain permission directly from the copyright holder. To view a copy of this licence, visit <http://creativecommons.org/licenses/by/4.0/>.

References

1. Çetinkaya C, Arabaci U (2006) Flash butt welding application on 16MnCr5 chain steel and investigations of mechanical properties. *Mater Des* 27(10):1187–1195. <https://doi.org/10.1016/j.matdes.2005.02.002>
2. Zhang F, Lv B, Hu B, Li Y (2007) Flash butt welding of high manganese steel crossing and carbon steel rail. *Mater Sci Eng A* 454–455:288–292. <https://doi.org/10.1016/j.msea.2006.11.018>

3. Bauri LF, Alves LHD, Pereira HB, Tschiptschin AP, Goldenstein H (2020) The role of welding parameters on the control of the microstructure and mechanical properties of rails welded using FBW. *J Market Res* 9(4):8058–8073. <https://doi.org/10.1016/j.jmrt.2020.05.030>
4. Li X, Ma R, Liu X, Lv Q, Wang X, Tian Z (2022) Effect of laser shock peening on fatigue properties of U75VG rail flash-butt welding joints. *Opt Laser Technol* 149. <https://doi.org/10.1016/j.optlastec.2022.107889>
5. Siddiqui MIH, Geleta DD, Bae G, Lee J (2020) numerical modeling of the inclusion behavior during AC flash butt welding. *ISIJ Int* 60(11):2503–2511. <https://doi.org/10.2355/isijinternational.ISIJINT-2020-143>
6. Zhang J, Zhang X, Li D, Lv Q, Ma R (2019) Extrusion behavior of impurities in upseting process of rail flash butt welding based on finite element method. *J Mater Res* 34(19):3351–3360. <https://doi.org/10.1557/jmr.2019.221>
7. Ma R, Huang D, Zhang J, Zhang Y, Lv Q (2020) Effects of rail flash-butt welding and post-weld heat treatment processes meeting different national standards on residual stresses of welded joints. *Int J Mater Res* 111(9):781–787
8. Kuroda T, Ikeuchi K, Ikeda H (2006) Flash butt resistance welding for duplex stainless steels. *Vacuum* 80(11–12):1331–1335. <https://doi.org/10.1016/j.vacuum.2006.01.068>
9. Xi C, Sun D, Xuan Z, Wang J, Song G (2016) Microstructures and mechanical properties of flash butt welded high strength steel joints. *Mater Des* 96:506–514. <https://doi.org/10.1016/j.matdes.2016.01.129>
10. Shen J et al (2018) Microstructure evolution and mechanical properties of flash butt-welded Inconel718 joints. *Mater Sci Eng A* 718:34–42. <https://doi.org/10.1016/j.msea.2018.01.104>
11. Li Y, Lin Z, Jiang A, Chen G (2003) Use of high strength steel sheet for lightweight and crashworthy car body. *Mater Des* 24(3):177–182. [https://doi.org/10.1016/S0261-3069\(03\)00021-9](https://doi.org/10.1016/S0261-3069(03)00021-9)
12. Ramachandran DC et al (2021) Role of bainitic microstructures with M-A constituent on the toughness of an HSLA steel for seismic resistant structural applications. *Mater Sci Eng A* 801. <https://doi.org/10.1016/j.msea.2020.140390>
13. Mosayebnezhad J, Sedighi M (2018) Numerical and experimental investigation of residual stresses in magnetically impelled arc butt welded joints in low alloy steels. *Int J Adv Manuf Technol* 96(9–12):4501–4515. <https://doi.org/10.1007/s00170-018-1865-5>
14. Kazasidis M et al (2021) Dissimilar welding between conventional and high strength low alloy naval steels with the use of robotic metal cored arc welding. *J Adv Manuf Technol* 113:2895–2907. <https://doi.org/10.1007/s00170-021-06819-8/Published>
15. Zhao D, Osipov A, Bezmelnitsyn A, Vdonin N, Liang D (2021) Statistical modeling and optimization of the resistance welding process with simultaneous expulsion magnitude consideration for high-strength low alloy steel. *J Adv Manuf Technol* 113:1173–1189. <https://doi.org/10.1007/s00170-021-06696-1/Published>
16. Basaeri A, Khorsand H, Eslami-Farsani R, Hasanniya MH (2020) Comparative experimental and numerical study on the mechanical properties, formability, and microstructure of two high strength steel sheets. *J Adv Manuf Technol* 108:2023–2033. <https://doi.org/10.1007/s00170-020-05399-3/Published>
17. Ziemian CW, Sharma MM, Whaley DE (2012) Effects of flashing and upset sequences on microstructure, hardness, and tensile properties of welded structural steel joints. *Mater Des* 33(1):175–184. <https://doi.org/10.1016/j.matdes.2011.07.026>
18. Shi SC, Wang WC, Ko DK (2022) Influence of inclusions on mechanical properties in flash butt welding joint of high-strength low-alloy steel. *Metals (Basel)* 12(2). <https://doi.org/10.3390/met12020242>
19. Wang X, Liu X, Zhang J, Deng J, Lv Q (2022) Numerical simulation of end face heating in alternating current flash butt welding based on electrical–thermal bidirectional coupling. *Int J Adv Manuf Technol* 120(1–2):173–183. <https://doi.org/10.1007/s00170-021-08599-7>
20. Xi CY, Sun DQ, Xuan ZZ, Wang JG, Song GS (2016) The effects of flash allowance and upset allowance on microstructures and mechanical properties of flash butt welded RS590CL steel joints. *J Mater Res* 31(24):3968–3980. <https://doi.org/10.1557/jmr.2016.403>
21. Lu P, Xu Z, Jiang K, Ma F, Shu Y (2017) Influence of flash butt welding parameters on microstructure and mechanical properties of HSLA 590CL welded joints in wheel rims. *J Mater Res* 32(4):831–842. <https://doi.org/10.1557/jmr.2016.509>
22. Shajan N, Arora KS, Shome M (2019) Correlation between grain misorientation, texture and impact toughness across a flash butt weld of HSLA steel. *Mater Lett* 236:436–439. <https://doi.org/10.1016/j.matlet.2018.10.153>
23. Shajan N, Arora KS, Sharma V, Shome M (2018) Effect of upset pressure on texture evolution and its correlation to toughness in flash butt joints. *Sci Technol Weld Joining* 23(5):434–440. <https://doi.org/10.1080/13621718.2017.1408197>
24. Shajan N, Arora KS, Asati B, Sharma V, Shome M (2018) Effects of post-weld heat treatment on the microstructure and toughness of flash butt welded high-strength low-alloy steel. *Metall Mater Trans A* 49(4):1276–1286. <https://doi.org/10.1007/s11661-018-4499-1>
25. Barooni O, Abbasi M, Givi M, Bagheri B (2017) New method to improve the microstructure and mechanical properties of joint obtained using FSW. *Int J Adv Manuf Technol* 93(9–12):4371–4378. <https://doi.org/10.1007/s00170-017-0810-3>
26. Abdollahzadeh A, Bagheri B, Abbasi M, Kokabi AH, Moghaddam AO (2021) Comparison of the weldability of AA6061-t6 joint under different friction stir welding conditions. *J Mater Eng Perform* 30(2):1110–1127. <https://doi.org/10.1007/s11665-020-05379-4>
27. Zolotarevsky NY, Rybin VV, Matvienko AN, Ushanova EA, Philippov SA (2019) Misorientation angle distribution of deformation-induced boundaries provided by their EBSD-based separation from original grain boundaries: case study of copper deformed by compression. *Mater Charact* 147:184–192. <https://doi.org/10.1016/j.matchar.2018.11.003>
28. Bagheri B, Abbasi M, Dadaei M (2020) Mechanical behavior and microstructure of AA6061-T6 joints made by friction stir vibration welding. *J Mater Eng Perform* 29(2):1165–1175. <https://doi.org/10.1007/s11665-020-04639-7>
29. Kapoor I, Lan Y, Rijkenberg A, Li Z, Janik V (2018) Quasi in-situ analysis of geometrically necessary dislocation density in α -fibre and γ -fibre during static recrystallization in cold-rolled low-carbon Ti-V bearing microalloyed steel. *Mater Charact* 145:686–696. <https://doi.org/10.1016/j.matchar.2018.09.032>
30. Ramesh R, Dinakaran I, Ravikumar R, Akinlabi ET (2020) Microstructural characterization and tensile behavior of Nd:YAG laser beam welded thin high strength low alloy steel sheets. *Mater Sci Eng A* 780. <https://doi.org/10.1016/j.msea.2020.139178>
31. Lee SI, Lee SY, Lee SG, Jung HG, Hwang B (2018) Effect of strain aging on tensile behavior and properties of API X60, X70, and X80 pipeline steels. *Met Mater Int* 24(6):1221–1231. <https://doi.org/10.1007/s12540-018-0173-9>
32. Lu Y et al (2022) Ex situ analysis of high-strength quenched and micro-alloyed steel during austenitising bending process: numerical simulation and experimental investigation. *Int J Adv Manuf Technol* 120(11–12):8293–8309. <https://doi.org/10.1007/s00170-022-09261-6>
33. Thewlis G (2004) Materials perspective: classification and quantification of microstructures in steels. *Mater Sci Technol* 20(2):143–160. Maney Publishing. <https://doi.org/10.1179/026708304225010325>

34. Soliman M (2020) Microstructural control and properties optimization of microalloyed pipeline steel. *Metals (Basel)* 10(11):1–22. <https://doi.org/10.3390/met10111499>
35. Grewal R, Aranas C, Chadha K, Shahriari D, Jahazi M, Jonas JJ (2016) Formation of Widmanstätten ferrite at very high temperatures in the austenite phase field. *Acta Mater* 109:23–31. <https://doi.org/10.1016/j.actamat.2016.02.062>
36. Xu Z, Lu P, Shu Y (2016) Microstructure and fracture mechanism of a flash butt welded 380CL steel. *Eng Fail Anal* 62:199–207. <https://doi.org/10.1016/j.engfailanal.2016.02.005>
37. Wang J, Ma C, Han J, Jiang Z, Linton V (2021) Acquisition of HSLA steel weld joints with excellent mechanical performance through flash butt welding physical simulation. *Mater Lett* 303. <https://doi.org/10.1016/j.matlet.2021.130511>
38. Bagheri B, Abdollahzadeh A, Abbasi M, Kokabi AH (2020) Numerical analysis of vibration effect on friction stir welding by smoothed particle hydrodynamics (SPH). *Arch Appl Mech* 90:2275–2296. <https://doi.org/10.1007/s00170-020-05839-0/Published>
39. Forsström A, Bossuyt S, Yagodzinsky Y, Tsuzaki K, Hänninen H (2019) Strain localization in copper canister FSW welds for spent nuclear fuel disposal. *J Nucl Mater* 523:347–359. <https://doi.org/10.1016/j.jnucmat.2019.06.024>
40. Lu Y et al (2021) Simulation, microstructure and austenite reconstruction of a medium carbon micro-alloyed steel subjected to an austenitising bending process. *Mater Lett* 305. <https://doi.org/10.1016/j.matlet.2021.130772>
41. Lavanya S, Mahadevan S, Mukhopadhyay CK (2019) Correlation of tensile deformation-induced strain in HSLA steel with residual stress distribution. *J Mater Eng Perform* 28(2):1103–1111. <https://doi.org/10.1007/s11665-019-3872-6>
42. Bagheri B, Abbasi M, Abdollahzadeh A, Kokabi AH (2020) Numerical analysis of cooling and joining speed effects on friction stir welding by smoothed particle hydrodynamics (SPH). *Arch Appl Mech* 90(10):2275–2296. <https://doi.org/10.1007/s00419-020-01720-4>

Publisher's note Springer Nature remains neutral with regard to jurisdictional claims in published maps and institutional affiliations.